4. Beamlines

This section describes the activity status of the light source and optics of the beamlines in FY2021. It includes the insertion device (ID), frontend, optics and transport channel, radiation shielding of SPring-8, and SACLA beamlines. In addition to routine maintenance, several component upgrades and R&D were performed. Beamline upgrade and portfolio rearrangement are ongoing toward the SPring-8 major upgrade. Some beamline reconstructions were carried out during this period.

1. Insertion device and frontend

1-1. Insertion device

In BL17SU, an undulator composed of both electromagnet and permanent magnet arrays has been used as an insertion device since 2002, which can generate synchrotron radiation with various polarization states. After nearly 20 years of operation, however, a malfunction has been found in one of the electromagnet coils (water leakage) in 2020, and its capabilities such as wavelength tunability and available polarization have been largely limited since then. After discussions on how to restore the device, we have decided to construct a new undulator instead of repairing the existing one because of many reasons; one of them is that a better solution to satisfy the users' demand in BL17SU has been proposed in 2011 [1], which is referred to as a "helical-8 undulator". The helical-8 undulator is based on a special magnetic circuit composed of two magnetic periods and enables two modes of operation: helical and figure-8 undulator modes. The former provides circularly polarized radiation whose helicity can be switched (from left-handed to right-handed), while the latter provides linearly (horizontally or vertically) polarized radiation. It should be stressed that the on-axis power density in the figure-8 mode is much lower than that of a conventional linear undulator, which is important for optical elements when the undulator deflection parameter (K value) should be high, as in the soft X-ray beamlines in SPring-8. In 2021, the design of the helical-8 undulator, including the magnetic period and dimensions of magnet blocks, was completed, and its construction is in progress.

1-2. Frontend

(1) High-heat-load handling techniques

To establish a method of predicting the fatigue crack growth life of GlidCop produced by a new process, we attempted to quantify the initial distribution of alumina-based inclusions, which are the starting point of fracture. The inclusions and their aggregates detected by analyzing cross-sectional structure images were evaluated for features representing geometric shape and distribution state. As a result, flat microinclusions (about 0.09 μm in width and 0.19 μm in depth) tend to be locally concentrated. In addition, statistical processing using the Weibull distribution on the aggregate structure, taking the height of an area-minimum circumscribed rectangle as a characteristic of the aggregate structure, suggested that an elliptical shape with a height of 100 μm and an aspect ratio of 1–10 should be defined as the initial defect of GlidCop.

(2) X-ray beam position monitor (XBPM)

We are working on the practical use of a pulse mode X-ray beam position monitor. The monitor is equipped with diamond heat sinks as blade-shaped

detection elements, and a micro-stripline structure as signal transmission lines, which generates a unipolar signal with a pulse length of approximately 1 ns FWHM. The improved monitor with an even higher heat resistance was installed in an insertion device beamline, and performance tests were conducted. As a result, long-term stable operation was confirmed without any heat resistance problems. It was also confirmed that the output of this monitor responds linearly to the electron beam motion excited by a beam shaker of the storage ring. The resolution of approximately 10 μm std was obtained in both horizontal and vertical directions for the electron bunch with a beam current of 0.9 mA/bunch. These results show the high practicality of this monitor.

(3) Energy-resolved beam monitoring system for X-ray beam exiting from the frontend

In the energy-resolved beam monitoring system installed at the downstream of the frontend in BL05XU, the diamond thin film as a scatterer was changed from polycrystalline to single crystalline in order to eliminate the noise of diffraction bright spots, resulting in extremely clear energy-resolved beam images. These images were in good agreement with the spatial distribution per energy calculated by SPECTRA; thus, this system can be the basis for the development of a method for the direct observation of the photon beam center without the influence of radiation from nearby bending magnets [2]. In addition, to make the photon beam position monitor having a practical throughput, we have started a feasibility study with a high-speed X-ray imaging detector, CITIUS [3]. CITIUS is developed by RIKEN and has a spectro-imaging capability. By using CITIUS, we have successfully obtained clearer energy-resolved beam images at a shorter exposure time.

2. Optics and transport channel

2-1. Commissioning of optics in upgraded BL09XU

BL09XU was reconstructed to a beamline dedicated to HAXPES applications at the end of FY 2020. New components, such as double channel-cut monochromators (DCCMs), X-ray phase retarders (XPRs), and monitoring systems, were installed as shown in Fig. 1. The commissioning was started in May 2021. Following the radiation survey, adjustments and performance evaluations of monitors, double-crystal monochromators (DCMs), channel-cut crystal monochromators (CCMs), DCCMs, and focusing optics were carried out. A low vibration level of 70 nrad in DCM was achieved by optimizing liquid nitrogen cooling conditions. A monolithic Wolter type-I focusing mirror has been installed at experimental hutch (EH) 1. A focusing size of 1.2 μm (vertical) × 20 μm (horizontal) was achieved. The high repeatability and easy alignment for focusing condition were also confirmed. A micro-focusing beam of 1 μm diameter was obtained by a K-B mirror at EH2 using a frontend slit as a virtual source. The commissioning was completed successfully, and the evaluations and test use of the end station began in June 2021.

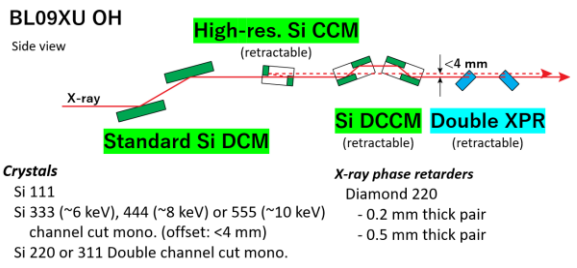

Fig. 1. Schematic drawing of optical layout in BL09XU optics hutch.

Table 1. Beam performance of DMM in BL20B2 EH1 and EH3.

DMM in BL20B2	EH1		EH3	
Energy	40 keV	110 keV	40 keV	110 keV
DMM optics	M1b-M2b	M1a-M2a	M1b-M2b	M1a-M2a
Beam size Horizontal x Vertical	62 x 4.0 mm^2	62 x 2.7 mm^2	300 x 20 mm^2	300 x 14 mm^2
Flux density	1.3 x 10^{12} phs/s/mm^2	3.9 x 10^{10} phs/s/mm^2	6.9 x 10^{10} phs/s/mm^2	1.6 x 10^{9} phs/s/mm^2

2-2. Commissioning of DCM and focusing mirror in upgraded BL35XU

BL35XU was reconstructed to a beamline dedicated to inelastic and nuclear resonant scattering (NRS) applications at the end of FY 2020. An air conditioning system for precise temperature control to stabilize the high-resolution monochromator for the NRS and a bent focusing optics system were newly installed in the optics hutch as shown in Fig. 2. The cryogenic cooling DCM was upgraded to reduce the thermal distortion of the crystals. The commissioning was started in April 2021. The heat load capacity of the DCM was improved from 350 W to 600 W, and the flux after the high-resolution monochromator was increased more than two times. The focusing size by the bent toroidal mirror was 21 μm (vertical) × 51 μm (horizontal) at EH1.

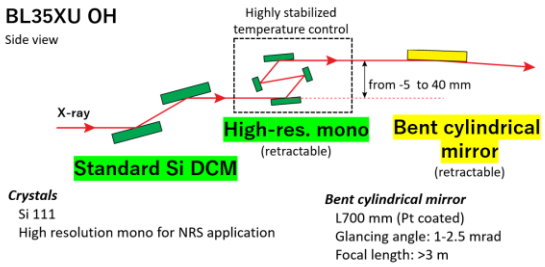

Fig. 2. Schematic drawing of optical layout in BL35XU optics hutch.

2-3. Commissioning of optics in upgraded BL20B2

In FY2020, double multilayer monochromators (DMMs) were designed and installed in the medium-length bending-magnet beamline BL20B2 to enhance the photon flux density around 40 keV and 110 keV for imaging applications such as the angiography of small animals and fossils, rocks, and industrial materials with a large field of view. The commissioning and performance evaluation of installed DMMs were started in April 2021 [4].

Two pairs of W/B_4C multilayer mirrors (M1a and M2a for 110 keV DMM, and M1b and M2b for 40 keV DMM) were installed in the optics hutch as shown in Fig. 3. The design parameters were reported in a previous annual report (FY2020). Filters were installed upstream of M1a to eliminate the total reflection component and also to reduce the heat load into the multilayer mirrors. 2-mm-thick SiC and 0.3-mm-thick Cu plates were used as filters for 40 keV and 110 keV, respectively.

The beam sizes and flux densities were measured at each experimental hutch (EH1 and EH3 are located at 44 m and 210 m from the source, respectively). The measured beam sizes and flux densities are shown in Table 1. Energy spectra of exit beams of DMMs were also measured at EH1.

The measured energy resolutions were 4.2% and 0.9% for 40 keV and 110 keV, respectively. The high-energy, high-flux, and large-area beams were available for the imaging applications.

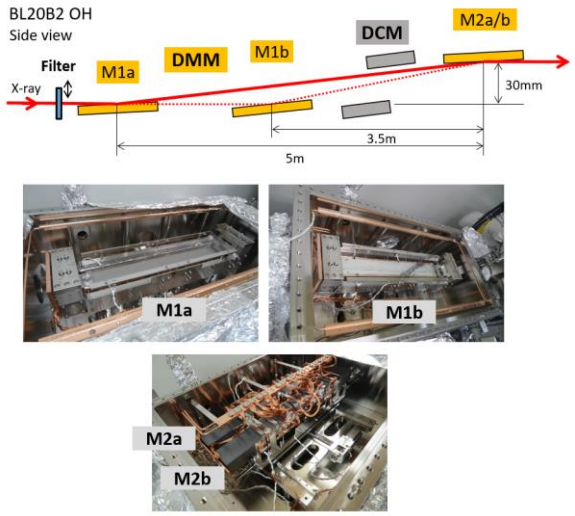

Fig. 3. Schematic drawing of optical layout and photographs of DMM in BL20B2 optics hutch.

2-4. Intense sub-microbeam of 100 keV obtained by laterally graded multilayer-coated focusing mirrors

An intense 100 keV DMM beam was used to achieve a high-flux micro-focused beam. Laterally graded multilayer mirrors in the K–B geometry (Fig. 4) were developed as a focusing optical element. The multilayers were formed by the multilayer coating system in SPring-8. As a result of evaluation at BL05XU, a 0.3 μm × 0.3 μm (FWHM) focused beam was obtained at an X-ray energy of 100 keV with a flux at 6 × 10 photons/s at a 1% energy bandwidth.

Fig. 4. Photograph of multilayer focusing mirrors in the K–B geometry for 100 keV X-rays.

2-5. Improvement in vibration analysis of double-crystal monochromators

Instability in the intensity and position of X-ray beams in an experimental hutch affects user experiments. Vibration in a DCM is one of the causes of this instability. The vibration violates the parallelism between the two crystals in a DCM, and the relative angular shifts fluctuate the intensity of the monochromatic beam.

The intensity fluctuation can be used to roughly estimate the vibration in a DCM. The intensity is monitored with a silicon PIN-photodiode. Intensity data averaged during 1 ms are obtained at a repetition rate of 1 kHz. When the first crystal of the DCM is stepped every 1 μrad, we obtain a stepped rocking curve convoluted by a fast-varying fluctuation caused by vibration, as shown in Fig. 5. Since a jump of the intensity corresponds to an angle of 1 μrad, the amount of fluctuation can be translated into angular vibration in the DCM at the half maximum of the rocking curve. The intensity fluctuation was estimated to be 888 nrad (standard deviation) in 2011. The amount was reduced to 107 μrad in 2020, by devising low-vibration flexible hoses, optimizing piping routes, and increasing stage rigidity. We are further improving designs of crystals and holders to suppress vibration less than

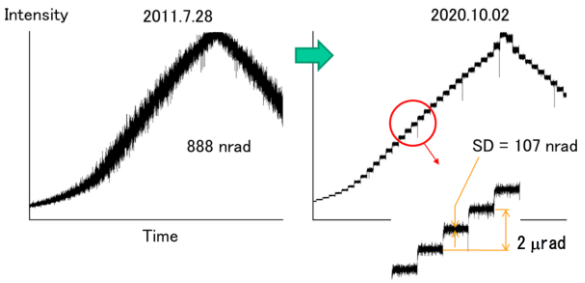

Fig. 5. Typical rocking curves contaminated by intensity fluctuation.

50 nrad..

The amount 107 nrad included the effect of intensity fluctuation of the incident beam into the DCM. The effect would be comparable to the vibration in the DCM. For a more precise analysis, we eliminate the effect of the incident beam by two procedures. One is the alignment of the incident frontend slit in several micrometer order to decrease the incident beam fluctuation. When the slit position is off axis, the measured rocking curves have spurious fluctuations, the amounts of which depend on the rotation angles of the first crystal. However, since the slit aperture is finite (typically 0.3 mm times 0.3 mm), the precise alignment alone is insufficient

As the second procedure, the DCM vibration is numerically extracted. Assuming that the vibration is static, the amount of intensity fluctuation caused by the DCM is proportional to the derivative of the rocking curve. The proportionality holds for every frequency component. Therefore, the power spectrum is proportional to the square of the derivative. We obtain a stepped rocking curve, calculate the power spectrum for every step, and extract the power spectrum corresponding to the square of the derivative by principal component analysis. Figure 6 shows the extracted spectra at BL09XU in May 2021. The vibrations were estimated to be approximately 70 nrad.

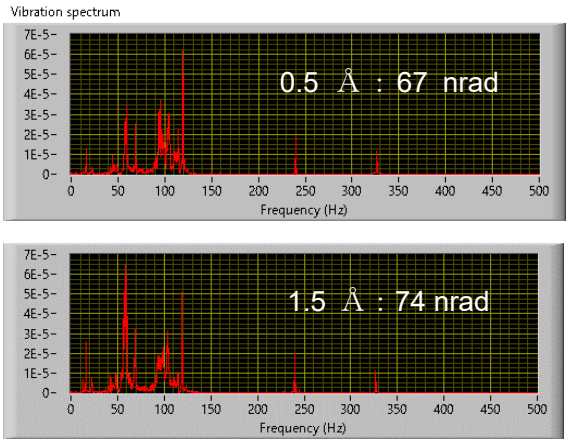

Fig. 6. Extracted spectra of DCM vibration for X-rays with wavelengths of 0.5 and 1.5 Å.

3. Radiation shielding for SPring-8 beamline

(1) Radiation shielding hutches

The conventional cable duct attached to a hutch is designed so that the cable can be taken in and out by opening and closing the lid. With this shape, it may not be possible to meet the demand for additional cable ducts in the narrow part of the hutch.

Therefore, a cable duct with a chicane-type maze structure and no movable lid was introduced into the BL13XU.

(2) Radiation-shielding calculations for applications to the Nuclear Regulation Authority

The 50th change permission application contained radiation-dose calculations for the construction of the frontend at BL48, the addition of the access mode at BL09XU, and the ID replacement of BL07LSU and BL17SU. The 51st change permission application contained radiation-dose calculations for the conversion of BL08W and the power up of BL31LEP.

(3) Radiation leakage inspection at beamlines

The following beamlines were inspected: BL01B1, BL09XU, BL20XU (reinstallation of local shield), BL09XU, BL20B2, and BL35XU (the 48th change permission).

(4) Radiation measurements and the development of methods

To investigate the radiation tolerance of the LED light and motor driver, GafChromic films were used for the dose measurement.

4. Beamlines of SACLA

4-1. XFEL beamlines

In FY2021, the two XFEL beamlines (BL2 and BL3) were stably operated in parallel to produce hard X-ray pulses in the range of 4–20 keV [5]. The main linac of SACLA drives the two beamlines by switching the electron-beam route in a pulse-by-pulse manner. Moreover, the switching operation was expanded to beam injection into the storage ring of SPring-8 [6]. SACLA has completely taken over the role of the conventional SPring-8 injector system since the spring of 2021. Both SACLA and SPring-8 have been operated steadily with the SACLA injection scheme.

For the XFEL transport channels, a new in-line spectrometer with an improved resolution has been proposed to monitor the XFEL spectra. The existing in-line spectrometer consists of a nano-diamond foil made by chemical vapor deposition (CVD) and an MPCCD detector. This spectrometer can provide information on peak photon energies with high accuracy. However, it is not suitable to measure a detailed spectral shape because the spectral resolution is low (~100 eV) and larger than the typical bandwidths of SASE-XFEL. Therefore, spectral width remains an uncontrollable characteristic in the accelerator-tuning method using machine learning techniques. To obtain single-shot spectra with an improved resolution, the new in-line spectrometer was designed to use a capillary filled with diamond microcrystals. In FY2021, a prototype of the spectrometer was installed at BL3 EH1 (Fig. 7(a)) [7]. Here, the spectral resolution is expected to be higher than 10 eV, as shown in Fig. 7(b), because of the larger grain size of the diamond. This prototype functioned as expected and would allow the optimization or even tuning of the spectral width.

After this success, a new spectrometer was fabricated for permanent installation in the transport channels at BL3. The new spectrometer can be operated either with the conventional nanodiamond

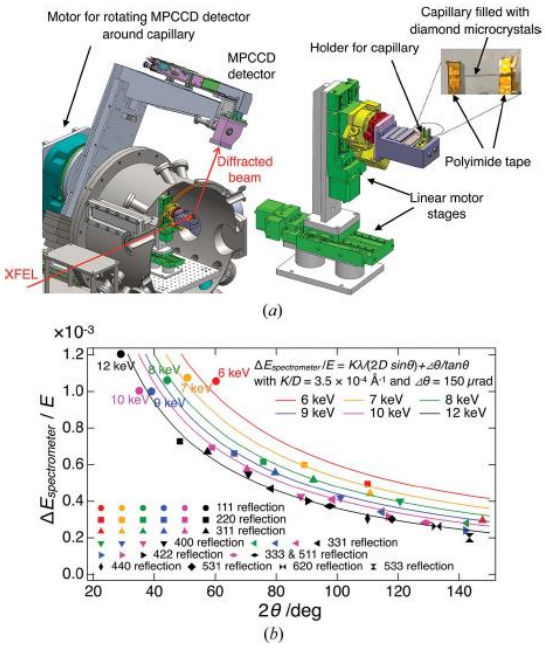

Fig. 7. (a) Schematic of spectrometer using diamond microcrystals in EH1 of SACLA BL3. (b) Energy resolution of spectrometer evaluated with monochromated XFEL pulses. Solid curves show the expected energy resolution of the spectrometer.

foil or the capillaries filled with microcrystals. The nanodiamond foil is suitable for a continuous monitor during experiments. The capillary is for the accelerator fine-tuning before every experiment. The installation of new spectrometers is planned in FY2022 at BL3 OH2 and BL2 OH1.

4-2. Soft X-ray FEL beamline

The soft X-ray (SX) FEL beamline (BL1) is driven by a dedicated 800 MeV linac (SCSS+) to produce SX pulses with photon energies of 40–150 eV and pulse widths of ~30 fs [8, 9]. The magnet degradation of the undulator caused a considerable decrease in output pulse energy (Fig. 8(a)). In March 2021, the first undulator unit was retuned to mitigate the magnet degradation, while the other two units were replaced with ones transferred from BL2 and BL3. After the work, pulse energies were successfully recovered as shown in Fig. 8(b). For instance, the pulse energies of 106 eV SXFEL were more than 50 μJ. The effects of the removal of undulator units from BL2 and BL3 were not significant for those XFEL beamline operations, because enough undulator units remain in the beamlines to reach saturation.

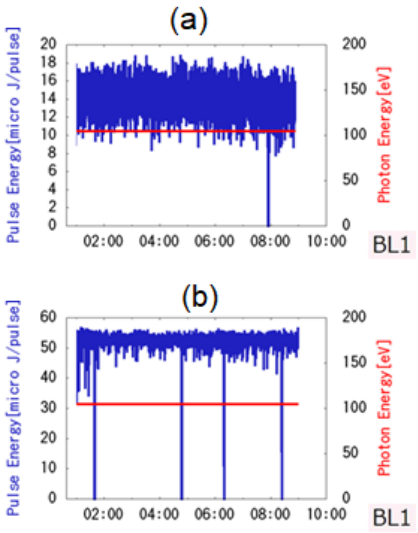

Fig. 8. Pulse energies of 106 eV FELs (a) before and (b) after replacement of undulators.

Tanaka Takashi[*1], Takahashi Sunao[*1], Ohashi Haruhiko[*2], Yamazaki Hiroshi[*2], Senba Yasunori[*2], Yumoto Hirokatsu[*2], Koyama Takahisa[*2], Takeshita Kunikazu[*2], Nariyama Nobuteru[*2], Goto Shunji[*2], Inubushi Yuichi[*3], Owada Shigeki[*3], Yabuuchi Toshinori[*3], Tono Kensuke[*3], and Yabashi Makina[*4]

*1 Innovative Light Source Division, RIKEN SPring-8 Center
*2 Light Source Division, JASRI
*3 XFEL Utilization Division, JASRI
*4 XFEL Research and Development Division, RIKEN SPring-8 Center

References

[1] Tanaka, T. & Kitamura, H. (2011). *Nucl. Instrum. Methods* **A659**, 537–542.
[2] Kudo, T. et al. (2022). J. Synchrotron Rad. 29, 670–676.
[3] Hatsui, T. et al., in preparation.
[4] Koyama, T. et al. (2022). J. Synchrotron Rad. 29, 1265–1272.
[5] Tono, K. et al. (2019). J. Synchrotron Rad. 26, 595–602.
[6] Hara, T. et al. (2021). Phys. Rev. Accel. Beams 24, 110702.
[7] Inoue, I. et al. (2022). J. Synchrotron Rad. 29, 862–865.
[8] Owada, S. et al. (2018). J. Synchrotron Rad. 25, 282–288.
[9] Owada, S. et al. (2020). J. Synchrotron Rad. 27, 1362–1365.